

# Quantifying and correcting geolocation error in sampling LiDAR forest canopy observations using high spatial accuracy ALS: A case study involving GEDI

Elliot S. Shannon<sup>1, 2</sup>, Andrew O. Finley<sup>1</sup>, Daniel J. Hayes<sup>3</sup>,  
Sylvia N. Noralez<sup>3</sup>, Aaron R. Weiskittel<sup>3</sup>, Bruce D. Cook<sup>4</sup>, Chad Babcock<sup>5</sup>

1. Department of Forestry, Michigan State University, East Lansing, MI, USA.
2. Department of Probability and Statistics, Michigan State University, East Lansing, MI, USA.
3. School of Forest Resources, University of Maine, Orono, ME, USA.
4. Biospheric Sciences Laboratory, NASA Goddard Space Flight Center, Greenbelt, MD, USA.
5. Department of Forest Resources, University of Minnesota, Saint Paul, MN, USA.

**Corresponding Author:** Andrew O. Finley, email: finleya@msu.edu.

## Abstract

Geolocation error in sampling LiDAR measurements of forest structure can compromise forest attribute estimates and degrade integration with georeferenced field measurements or other remotely sensed data. Integrating sampling LiDAR with other georeferenced data is especially problematic when geolocation error is not well quantified. Here, we propose and illustrate a model that uses high spatial accuracy airborne laser scanning (ALS) data from

NASA Goddard’s LiDAR, Hyperspectral & Thermal Imager (G-LiHT) to quantify and correct geolocation error in NASA’s Global Ecosystem Dynamics Investigation (GEDI) space-borne sampling LiDAR. The model accommodates multiple canopy height metrics derived from a simulated GEDI footprint kernel of known functional form using spatially coincident G-LiHT, and incorporates both additive and multiplicative mapping between the canopy height metrics generated from both LiDAR datasets. A Bayesian implementation provides probabilistic uncertainty quantification in both parameter and geolocation error estimates. Results show an estimated maximum a posteriori (MAP) systematic geolocation error (i.e., across all GEDI footprints) of 9.62 m in the southwest direction. In addition, estimated MAP actual geolocation errors (i.e., within GEDI footprints) were highly variable with results showing a  $\sim 0.15$  probability the true GEDI footprint center is within 10 m and a  $\sim 0.45$  probability the true GEDI footprint center is within 20 m. Estimating and correcting geolocation error via the modeling approach outlined here can help inform subsequent efforts to integrate sampling LiDAR, like GEDI, with other georeferenced data.

## Highlights

- A novel model to partition sampling LiDAR systematic and actual geolocation error.
- Independent GEDI geolocation error assessment with uncertainty quantification.
- Highlight important distinctions between systematic and actual geolocation error.

## 1 Introduction

Models of forest attributes such as aboveground biomass (AGB) have become important tools for monitoring forest carbon storage and sequestration. To this end, accurate measurements of forest structure represent an invaluable resource for both research and management of forest ecosystems. Traditionally, sampling techniques including field surveys and airborne laser

scanning (ALS) campaigns have provided detailed measurements of 3D forest structure, often with relatively small geolocation error. However, these measurements are typically limited in their temporal and spatial extent due to high acquisition cost. Now, several spaceborne LiDAR campaigns provide forest structure measurements at nearly global extent, allowing new opportunities for multi-sensor data fusion in AGB models. However, the geolocation error of measurements from these spaceborne sensors can be large and not well quantified, leading to increased uncertainty in model estimates. Given this trade-off, models of forest structure can benefit from incorporating both airborne and spaceborne LiDAR data, with careful consideration given to their integration (Silva et al., 2021).

NASA’s Global Ecosystem Dynamics Investigation (GEDI) LiDAR mission provides spaceborne measurements of forest structure along the orbital path of the International Space Station (ISS). GEDI samples 25 m footprints of high resolution waveform LiDAR, providing 3D measurements of the Earth’s surface including ground elevation, forest canopy height, and forest canopy cover (Dubayah et al., 2020). Since its launch in December of 2018, GEDI data have been extensively used for applications such as carbon monitoring and forest AGB estimation (Saarela et al., 2018; Silva et al., 2021; Duncanson et al., 2022), often informed using ancillary remote sensing and field data. Specifically, relative height (RH) metrics, which represent the vertical distribution of forest canopy heights above ground, are calculated by GEDI at a number of percentiles across the canopy elevation profile, and serve as key explanatory covariates in AGB models. By repeatedly sampling transects along the ISS orbit, GEDI’s extensive spatial coverage provides great opportunity for modeling applications over large scales.

Goddard’s LiDAR, Hyperspectral, and Thermal Imager (G-LiHT) is a multi-sensor, airborne remote sensing system that, like GEDI, uses LiDAR technology to map forest vertical structure including RH metrics (Cook et al., 2013). As an airborne instrument, the temporal and geographic extent of G-LiHT acquisitions are limited compared to spaceborne missions such as GEDI. However, G-LiHT’s airborne LiDAR scanner can acquire and discretize a

higher sample density ( $\sim 12$  pulses  $\text{m}^2$ ) of small footprint laser pulses ( $\sim 10$  cm diameter) to create a continuous, canopy height surface layer model at 1 m horizontal spatial resolution. Individual discrete return measurements used to compute vertical canopy heights and forest RH metrics had a positional error of  $< 10$  cm between repeat acquisitions.

Characterizing footprint-level GEDI geolocation error is a crucial step when integrating its data with other sensor data and field measurements for applications such as AGB estimation and mapping. Over time, the geolocation error associated with GEDI’s footprint-level measurements has been improved, and currently the geolocation error for Version 2 GEDI data is estimated to be  $\sim 10$  m (Dubayah et al., 2020). Although this marks a great improvement over previous versions of the GEDI datasets, remaining geolocation errors such as these may undermine forest canopy height retrievals in areas of complex or heterogeneous forest structure (Frazer et al., 2011; Milenković et al., 2017; Roy et al., 2021) and thus hinder identification of coincident measurements with field plot and ALS datasets (Duncanson et al., 2022). To this end, previous studies have implemented a variety of methods to characterize or even correct the geolocation uncertainty of GEDI and improve estimates of terrain and canopy heights (Liu et al., 2021; Quirós et al., 2021; Roy et al., 2021; Wang et al., 2022). In these studies, coincident ALS data with smaller estimated geolocation errors are compared with GEDI metrics to assess disagreements between the reported GEDI RH metrics and observed ALS data, often via simulation to allow direct comparison. For example, in a waveform interpretation study, Lang et al. (2022) first implemented a geolocation correction step to optimally correlate simulated GEDI waveforms with ALS data. Here, Version 1 GEDI data were corrected in blocks, with an initial estimated mean horizontal positioning error of  $\sim 20$  m, which was reduced to only a few meters on average using the method outlined in Hancock et al. (2019). Similarly, Wang et al. (2022) compared the root mean squared error (RMSE) values of GEDI performance with and without colocation calibration, and observed increased uncertainty in estimated top of canopy RH values for uncalibrated footprints. Therefore, quantification or correction of geolocation error is crucial for propagating



measurement uncertainty and improving model estimates of forest attributes such as AGB (Wang et al., 2022).

In a previous study, Liu et al. (2021) used discrete return ALS data to simulate GEDI waveforms over a range of potential horizontal offsets, and quantified GEDI’s geolocation error using the offset with the highest correlation between waveforms. This waveform matching approach resulted in slight improvements in both RMSE and mean absolute error (MAE) values for GEDI terrain height estimates. Similarly, Quirós et al. (2021) assessed the positional error of reported GEDI footprint locations using ALS data by considering 16 positional adjustments at distances of 5 or 10 m in the along and across track directions, as well as at intermediate angular positions. Here, the position resulting in the lowest RMSE was considered optimal, and the authors observed a consistent improvement in RMSE of estimated ground elevations for positional adjustments of  $270^\circ$  within 10 m. These studies highlight the dual sources of geolocation error associated with spaceborne LiDAR measurements such as GEDI, which might result from both biases in the instrument itself, along with random noise at the level of individual footprints. Therefore, assessments of geolocation error should aim to identify systematic shifts in footprint-level measurements that improve agreement with ALS measurements, while incorporating flexibility to capture location specific effects.

Other studies have also investigated the impacts of geolocation error on measurements of forest canopy height. Roy et al. (2021) used a Monte Carlo simulation technique to randomly generate positional errors of GEDI footprints from ALS data in the Congo. They found the impact of geolocation error on GEDI canopy height retrieval was dependent on local spatial variation in forest canopy height. In this way, spaceborne canopy height measurements of complex and fragmented forests may be more greatly impacted by geolocation error than those of more homogeneous forest types (Milenković et al., 2017). As forests become more heterogeneous following increased disturbances and diverse management practices, statistical methods are urgently needed to assess the effect of geolocation error and propagate its associated uncertainty to estimates of forest attributes derived from spaceborne LiDAR

data.

In this paper we propose and illustrate a model that uses high spatial accuracy ALS data to quantify and correct geolocation error in forest canopy measurements from larger footprint sampling LiDAR. Using this model, we aim to learn about both location specific and systematic (i.e., across locations) geolocation error using spatially-coincident ALS data. The proposed model: 1) uses a sampling LiDAR footprint kernel of known functional form with parameters that can be fixed or estimated; 2) considers multiple canopy metrics at each footprint location; 3) estimates additive and multiplicative mapping between canopy metrics generated from the two LiDAR data sources; 4) yields key summaries of geolocation error within and across locations where both LiDAR data sources are observed; 5) provides probabilistic uncertainty quantification in parameter and geolocation error estimates; and 6) extends in a straightforward way to accommodate geolocation error that might be non-stationary in space and/or time (e.g., settings where geolocation error might vary based on acquisition location or time).

While the proposed modeling framework is general and might be applied in a variety of settings, we motivate the method’s exposition using the GEDI and G-LiHT data described in Section 2. The proposed model is presented in Section 3. Here, too, we define a submodel and criterion to assess model fit and describe how we characterize geolocation error. Analysis results are presented in Section 4, which is followed by a discussion of results in Section 5. Some model extensions are described in Section 6, along with concluding remarks and next steps.

## 2 Data

### 2.1 Study area

The NASA Carbon Monitoring System (CMS) Maine study site is located in Northern Maine, USA (Figure 1a). As a unit of the North American Forest Dynamics Project (Goward et al.,

2008), the Maine CMS area has been closely monitored via airborne and field forest inventories for nearly a decade (Deo et al., 2017). Most recently, ALS data coincident with GEDI spaceborne measurements were captured over the Maine CMS area (Figure 1b). The area is composed of a mix of both hardwood and softwood tree species and has a complex structure reflecting the unique disturbance history of varied logging and management strategies. These dynamic harvest patterns have created a diverse forest canopy structure across the study site, with both fine and coarse scale forest canopy gaps present (Figure 1c). This fine-scale heterogeneity may exacerbate any potential disagreement between spaceborne and airborne canopy height measurements caused by geolocation error (Milenković et al., 2017).

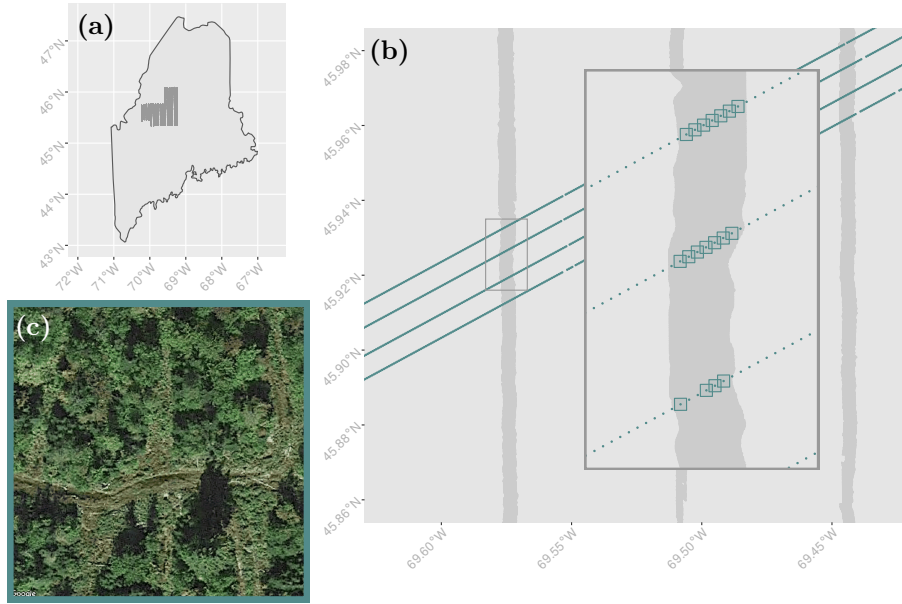


Figure 1: (a) Regional view of the Maine CMS study area, with G-LiHT airborne LiDAR acquisition tracks oriented in the north-south direction. (b) Sample of unfiltered spaceborne GEDI LiDAR data (green) captured over the G-LiHT acquisition tracks, with 70 m square buffers generated for spatially coincident, high-quality GEDI observations. (c) Satellite imagery for a single, high-quality GEDI observation with 70 m square buffer.

## 2.2 GEDI data

Version 2 Global Footprint Level GEDI L2A Elevation and Height Metrics data were downloaded from the USGS Land Processes Distributed Active Archive Center (LP DAAC) Data

Pool using a spatial query through NASA’s Common Metadata Repository (CMR) (see Supplementary Material for detailed data download and processing steps). The GEDI L2A dataset represents a spaceborne LiDAR campaign to capture full waveform LiDAR data globally with a footprint diameter of  $\sim 25$  m and estimated geolocation error of  $\sim 10$  m (Dubayah et al., 2020). The GEDI data are reported as a collection of RH metrics at 100 percentiles, along with quality flags, and unique identifiers for each footprint. Given the estimated  $\sim 10$  m geolocation error of the Version 2 GEDI data, along with the  $\sim 12.5$  m radius of the GEDI footprint, a square focal area of side-length 45 m was centered around each reported GEDI footprint center. This focal area was taken as the search domain to capture the full extent of the possible “true” GEDI footprint center locations, and suggests that the “true” GEDI footprint location is within 22.5 m in the  $x$  (easting) and  $y$  (northing) directions from the reported footprint center.

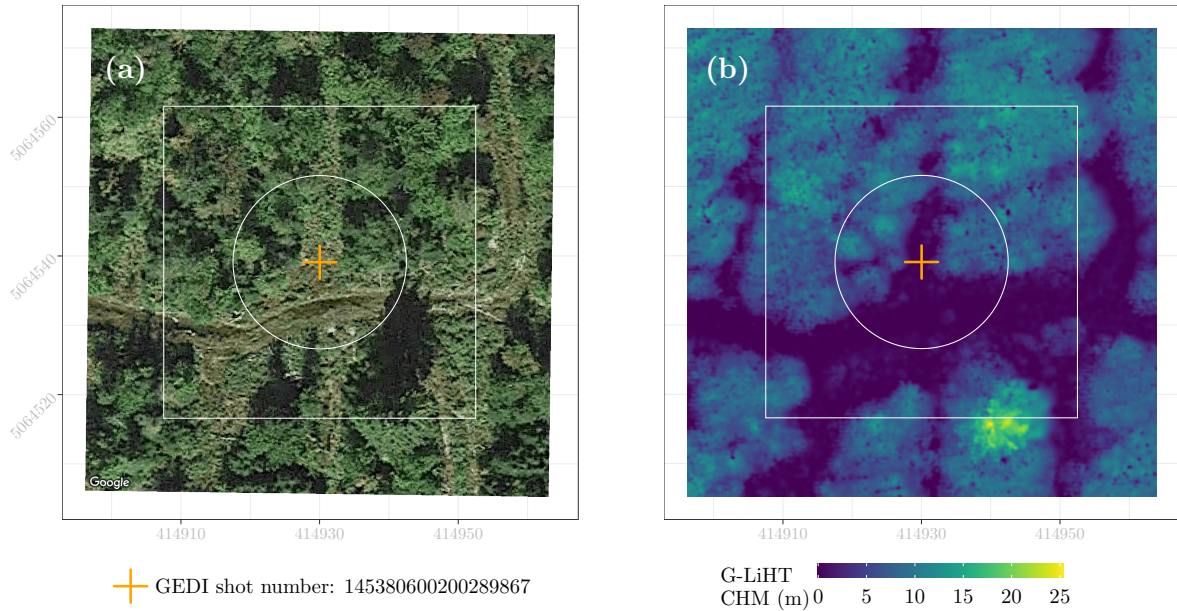


Figure 2: (a) Satellite imagery for a single reported GEDI footprint, with 45 m square focal area. The “GEDI shot number” is the unique footprint identifier provided with LP DAAC data. (b) G-LiHT canopy height model (CHM) generated from the 3D point cloud measurements for the same focal area displayed in (a).

In Figure 2a, the footprint center for a single GEDI shot is displayed as an orange

cross-hairs within the 25 m diameter circular footprint. The square surrounding the GEDI footprint represents the 45 m square focal area (search domain). The total spatial extent of Figure 2a represents the 70 m square buffer, from which G-LiHT ALS point cloud data can be used to simulate GEDI within the smaller focal area.

### 2.2.1 Quality filtering

The Version 2 GEDI L2A data were filtered according to the recommendations outlined in the GEDI Level 2 User Guide (Dubayah et al., 2021). Specifically, GEDI data were filtered to include only measurements taken by the power beams, nighttime acquisitions, and quality flag value of 1. To ensure that the GEDI data were collected during leaf-on conditions, only GEDI data collected during the 2021 growing season (months of June, July, and August) were considered. Finally, only GEDI footprints with square buffers coinciding with the ALS transects were retained (Figure 1b). In total, 222 GEDI shots were considered for this study, all of which were collected on July 7, 2021 due to the strict filtering criteria considered here. By only considering high-quality GEDI footprints collected during a single day, effects of temporal variability in the GEDI measurement quality and geolocation error due to factors such as orbital path, cloud cover, atmospheric conditions, and temporal misalignment with the G-LiHT ALS data should be minimized.

## 2.3 G-LiHT ALS data

G-LiHT data were collected over the Maine CMS study area between July 27 and August 6, 2021, along 16 established north-south transects (Figure 1a)(Cohen et al., 2020). The G-LiHT data were delivered as individual LiDAR returns in the form of a 3D point cloud, including classified ground returns and vertical measurements interpreted as height above the interpolated ground surface, with a sampling density up to 12 laser pulses/m<sup>2</sup>. Repeat acquisitions of buildings, road surfaces, and ground beneath forest canopies demonstrated 10 cm ( $1\sigma$ ) accuracy and precision following GPS-INS post-processing and boresight alignment.

Figure 2b illustrates the G-LiHT point cloud derived canopy height model (CHM) for the example focal area introduced in Section 2.2.

## 2.4 Simulation

GEDI RH metrics were simulated from the G-LiHT point cloud data via the approach outlined in Hancock et al. (2019). Here, GEDI RH metrics were calculated using a Gaussian-weighting of G-LiHT point cloud measurements within the 25 m GEDI footprint, with weighting parameters adopted to reflect the GEDI footprint kernel (see Equation 1 in Hancock et al., 2019). For a reported GEDI footprint, 10,000 simulations were generated within the 45 m square focal area, resulting in a dense  $\sim 0.45$  m grid. Specifically, for a single simulated footprint centered at  $\ell = (\ell_1, \ell_2)$  (with  $\ell_1$  and  $\ell_2$  being easting and northing coordinates, respectively), the weight  $w(\cdot)$  of a proximate 3D G-LiHT point  $i = (x_i, y_i, z_i)$  is calculated as

$$w(i) = \frac{1}{\sigma_f \sqrt{2\pi}} e^{-0.5 \frac{(x_i - \ell_1)^2 + (y_i - \ell_2)^2}{\sigma_f^2}} \quad (1)$$

where  $\sigma_f$  is the Gaussian kernel decay parameter (here,  $\sigma_f = 5.5$  m to give  $> 97\%$  of the total weight to points within 12.5 m of the GEDI footprint center) and  $x_i$  and  $y_i$  specify the easting and northing coordinates of point  $i$ , respectively. In this way, G-LiHT ALS points at the center of the simulated footprint were given the greatest weight, with decreasing weight as distance increases from the footprint center. Next, each  $z_i$  (giving the RH value of G-LiHT point  $i$  in meters) was scaled by its corresponding  $w(i)$  as calculated in (1), and then standardized by  $\sum_{i=1}^h z_i \times w(i)$ , where  $h$  is the total number of G-LiHT points within 12.5 m of  $\ell(\mathbf{s})$ . The  $z_i$  values were then ordered by their scaled RH values. Finally, the  $p^{th}$  simulated RH percentile value was calculated as the smallest  $z_i$  value  $\geq p\%$  of the scaled relative  $z$  heights. This method serves as an implementation of simulator  $g(\cdot)$  as described in Section 3, and produces results comparable to the method described in Hancock et al. (2019).

### 3 Models

Here we consider models for buffer areas where both GEDI and ALS (i.e., G-LiHT) spatially coincide. Our model notation uses bold terms for vectors and non-bold terms for scalars. The term  $\mathbf{s}$  is a coordinate vector (i.e.,  $\mathbf{s} = (s_1, s_2)$  with  $s_1$  and  $s_2$  being easting and northing coordinates, respectively) and when given without a subscript it is considered a generic GEDI footprint center location. Terms followed by  $\mathbf{s}$  in parentheses reference a location specific value of the given term. The posited model is

$$\mathbf{z}(\mathbf{s}) = \boldsymbol{\alpha} + \boldsymbol{\beta} \odot g(\boldsymbol{\ell}(\mathbf{s}), \boldsymbol{\theta}; \text{Data}(\mathbf{s})) + \boldsymbol{\epsilon}(\mathbf{s}), \quad (2)$$

$$\boldsymbol{\ell}(\mathbf{s}) = \boldsymbol{\mu}_{\ell} + \boldsymbol{\epsilon}_{\ell}(\mathbf{s}), \quad (3)$$

where the outcome vector  $\mathbf{z}(\mathbf{s}) = (z_1(\mathbf{s}), z_2(\mathbf{s}), \dots, z_m(\mathbf{s}))^\top$  comprises  $m$  canopy measurements at location  $\mathbf{s}$  (e.g., recorded GEDI RH metrics at  $m$  percentiles),  $\boldsymbol{\alpha} = (\alpha_1, \alpha_2, \dots, \alpha_m)^\top$  and  $\boldsymbol{\beta} = (\beta_1, \beta_2, \dots, \beta_m)^\top$  are parameter vectors to be estimated,  $g(\cdot)$  is a function that returns a vector of length  $m$  that approximates  $\mathbf{z}(\boldsymbol{\ell}(\mathbf{s}))$  at geographic location  $\boldsymbol{\ell}(\mathbf{s}) = (\ell_1(\mathbf{s}), \ell_2(\mathbf{s}))^\top$  using a set of parameters  $\boldsymbol{\theta}$  and high spatial accuracy data (i.e.,  $\text{Data}$ ) that cover the region over locations  $\mathbf{s}$  and  $\boldsymbol{\ell}(\mathbf{s})$  (view  $\boldsymbol{\ell}(\mathbf{s})$  as a coordinate vector at or around  $\mathbf{s}$ ). For example,  $\text{Data}$  could be G-LiHT or similar ALS data used by  $g(\cdot)$  to simulate GEDI RH metrics. The vector  $\boldsymbol{\theta}$  holds parameters used by  $g(\cdot)$  to map information in  $\text{Data}(\mathbf{s})$  to elements of  $\mathbf{z}(\mathbf{s})$ . For example,  $\boldsymbol{\theta}$  could hold information about the GEDI footprint radius and kernel decay parameter  $\sigma_f$  (see, e.g., Figure 3 for an illustration of  $g(\cdot)$  for the simulator described in Section 2.4). The  $\odot$  operator denotes component-wise multiplication between the left and right operand vectors. Parameter vectors  $\boldsymbol{\alpha}$  and  $\boldsymbol{\beta}$  provide additive and multiplicative adjustments, respectively, to the  $m$  outputs of  $g(\cdot)$ . The elements of the residual vector  $\boldsymbol{\epsilon}(\mathbf{s}) = (\epsilon_1(\mathbf{s}), \epsilon_2(\mathbf{s}), \dots, \epsilon_m(\mathbf{s}))^\top$  follow a zero centered normal distribution  $N(0, \tau_j^2)$  for  $j = (1, 2, \dots, m)$ .

As defined in (3), the coordinate vector  $\boldsymbol{\ell}(\mathbf{s})$  has mean vector  $\boldsymbol{\mu}_{\ell} = (\mu_{\ell,1}, \mu_{\ell,2})^\top$  and error

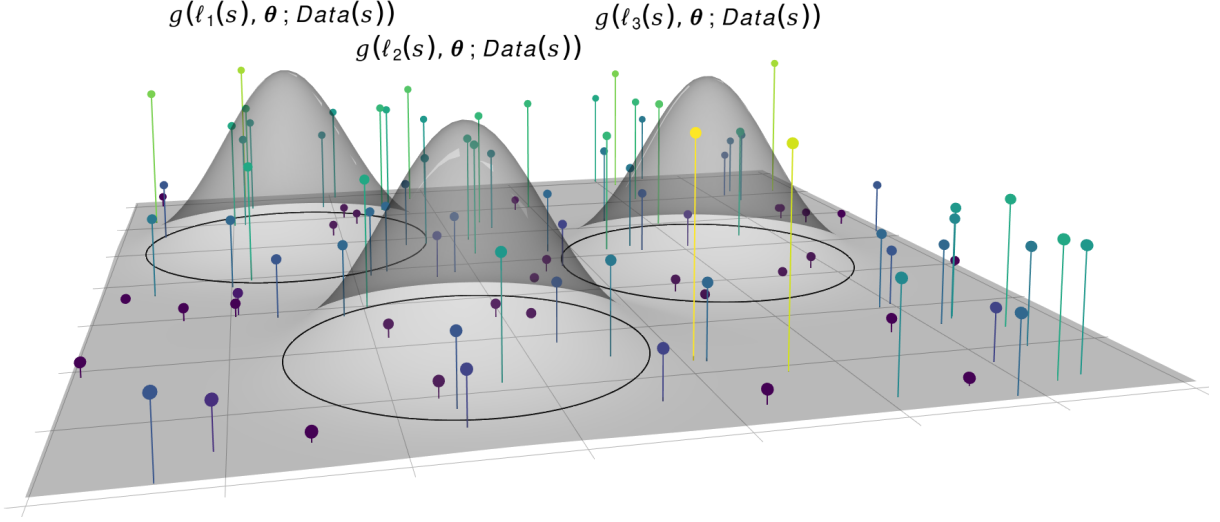


Figure 3: A sample of G-LiHT point cloud measurements ( $Data(s)$ ) for a 70 m square buffer around a reported GEDI footprint location (centered at  $s$ ) with three simulated footprint locations and their associated Gaussian kernel point weightings. Each kernel illustrates the function  $g(\cdot)$  used to simulate GEDI RH metrics at location  $\ell_i(s)$  with parameter set  $\theta$  (see Section 3).

vector  $\epsilon_\ell(s)$  with elements that follow a zero centered normal distribution  $N(0, \sigma_{\ell,k}^2)$  for  $k = (1, 2)$ .

A local coordinate system is used for each of the  $n$  GEDI footprint locations. This coordinate system places  $s_i$ , for  $i = (1, 2, \dots, n)$ , at the center of a 70-by-70 meter square buffer (i.e., each  $s_i$  is transformed from its original coordinates to  $(35, 35)$ ). The rationale for choosing this region extent is described in Section 2. This coordinate system, which is common among locations, allows  $\mu_\ell$  to be interpreted as the location that minimizes the residual variance between all observed  $z(s_i)$ s and estimated  $\ell(s_i)$ s. Then, variance parameters  $\sigma_{\ell,1}^2$  and  $\sigma_{\ell,2}^2$  capture the easting and northing variance of all  $\ell(s_i)$ s about  $\mu_\ell$ . While these summary parameters are insightful, we also compute a maximum a posteriori probability (MAP) estimate for each  $\ell(s)$ , denoted as  $\eta_\ell(s)$ , and a composite MAP estimate over all  $n$  focal areas, denoted as  $\eta_\ell$ . Here,  $\eta_\ell(s)$  is the largest valued mode of  $\ell(s)$ 's posterior distribution, and  $\eta_\ell$  is the largest valued mode of the posterior distribution accumulated over



all  $\ell(\mathbf{s})$ s (in the same way that  $\boldsymbol{\mu}_\ell$  is the mean vector over all  $\ell(\mathbf{s})$ s). The distance between a given  $\boldsymbol{\eta}_\ell(\mathbf{s})$  and  $\mathbf{s}$  is used to quantify location specific deviation between the estimated and reported GEDI footprint center location. In the same way, the distance between  $\boldsymbol{\eta}_\ell$  and  $\mathbf{s}$  is used to quantify systematic deviation between estimated and reported GEDI footprint center locations across all observed focal areas.

Model parameters in (2) were estimated using a Bayesian approach, see, e.g., Gelman et al. (2013). Canopy height metrics from the  $n$  locations were stacked into a  $nm$  length vector  $\mathbf{z} = (\mathbf{z}(\mathbf{s}_1)^\top, \mathbf{z}(\mathbf{s}_2)^\top, \dots, \mathbf{z}(\mathbf{s}_n)^\top)^\top$  and parameter input to  $g(\cdot)$  was stacked into a  $2n$  length vector  $\boldsymbol{\ell} = (\boldsymbol{\ell}(\mathbf{s}_1)^\top, \boldsymbol{\ell}(\mathbf{s}_2)^\top, \dots, \boldsymbol{\ell}(\mathbf{s}_n)^\top)^\top$ . For this analysis we assumed elements in  $\boldsymbol{\theta}$  were known and fixed; however, they could be estimated if desired (see Section 2.4 for the definition of  $g(\cdot)$  and  $\boldsymbol{\theta}$  values). Following (2) and (3), the parameters' joint posterior distribution  $p(\boldsymbol{\alpha}, \boldsymbol{\beta}, \boldsymbol{\tau}, \boldsymbol{\ell}, \boldsymbol{\mu}_\ell, \boldsymbol{\sigma}_\ell | \mathbf{z}, \boldsymbol{\theta}, \text{Data})$ , where  $\boldsymbol{\tau} = (\tau_1^2, \tau_2^2, \dots, \tau_m^2)^\top$ ,  $\boldsymbol{\sigma}_\ell = (\sigma_{\ell,1}^2, \sigma_{\ell,2}^2)^\top$ , and all other parameters were previously defined, is proportional to the likelihood times the prior distributions

$$\begin{aligned}
& \prod_{i=1}^n \prod_{j=1}^m \underbrace{N(z_j(\mathbf{s}_i) | \alpha_j + \beta_j g_j(\boldsymbol{\ell}(\mathbf{s}_i); \boldsymbol{\theta}, \text{Data}(\mathbf{s}_i)), \tau_j^2)}_{\text{Likelihood}} \times \\
& \prod_{j=1}^m N(\alpha_j | \mu_\alpha, \sigma_\alpha^2) \times \prod_{j=1}^m N(\beta_j | \mu_\beta, \sigma_\beta^2) \times \prod_{j=1}^m IG(\tau_j^2 | a_\tau, b_\tau) \times \\
& \prod_{i=1}^n \prod_{k=1}^2 N(\ell_k(\mathbf{s}_i) | \mu_{\ell,k}, \sigma_{\ell,k}^2) \times \prod_{k=1}^2 N(\mu_{\ell,k} | s_k, \sigma_{\mu_\ell,k}^2) \times \prod_{k=1}^2 IG(\sigma_{\ell,k}^2 | a_\ell, b_\ell).
\end{aligned} \tag{4}$$

Hyperparameters for the prior distributions in (4) were chosen to be weakly informative. Specifically, we assigned a normal ( $N$ ) prior distribution to elements of the likelihood's additive adjustment vector  $\boldsymbol{\alpha}$  with mean  $\mu_\alpha = 0$  and variance  $\sigma_\alpha^2 = 1,000$ . Similarly, elements in the multiplicative adjustment vector  $\boldsymbol{\beta}$  are assigned a normal prior distribution with mean  $\mu_\beta = 1$  and variance  $\sigma_\beta^2 = 1,000$ . Notice, prior means of 0 and 1 for elements of  $\boldsymbol{\alpha}$  and  $\boldsymbol{\beta}$ , respectively, places some weight on the prior belief that the output of  $g(\cdot)$  does not need additive or multiplicative adjustment, although the large variances allow for

substantial learning from the data. Elements in the likelihood’s variance parameter vector  $\boldsymbol{\tau}$  each follow an inverse-Gamma (*IG*) prior distribution with shape and scale hyperparameters  $a_\tau = 2$  and  $b_\tau = 10$ , respectively. For the *IG*, when the shape equals 2, the distribution’s mean equals the scale and its variance is infinite. Here, we chose a scale equal to 10 from exploratory analysis using linear regression defined by the simplified likelihood  $\prod_{i=1}^n \prod_{j=1}^m N(z_j(\mathbf{s}_i) | g_j(\mathbf{s}_i; \boldsymbol{\theta}, \text{Data}(\mathbf{s}_i)), \tau_j^2)$  (i.e., assuming no geolocation error nor additive and multiplicative adjustment). The induced prior on the easting and northing components in  $\boldsymbol{\ell}(\mathbf{s}_i)$  are normal with mean  $\mu_{\ell,1}$  and  $\mu_{\ell,2}$  and variances  $\sigma_{\ell,1}^2$  and  $\sigma_{\ell,2}^2$ , respectively. We set the hyperprior distributions for  $\mu_{\ell,1}$  and  $\mu_{\ell,2}$  (i.e., elements of  $\boldsymbol{\mu}_\ell$ ) as normal with means  $s_1$  and  $s_2$  and variances  $\sigma_{\mu_{\ell,1}}^2 = \sigma_{\mu_{\ell,2}}^2 = 1,000$ . Notice, given the common local coordinate system,  $\mathbf{s} = (s_1, s_2)$  equals (35, 35) for all focal areas. Said differently, we are setting the prior mean for  $\boldsymbol{\ell}(\mathbf{s}_i)$  equal to  $\mathbf{s}_i$  to reflect prior belief that the reported location  $\mathbf{s}_i$  for the GEDI footprint is accurate, but allowing a larger variance so data can inform estimates of  $\boldsymbol{\ell}(\mathbf{s})$ s. Lastly, hyperprior distributions for  $\sigma_{\ell,1}^2$  and  $\sigma_{\ell,2}^2$  are *IG* with  $a_\ell = 2$  and  $b_\ell = 100$ . This choice of *IG* scale expresses prior belief that  $\boldsymbol{\ell}(\mathbf{s})$ s have a standard deviation of 10 meters about  $\boldsymbol{\mu}_\ell$ ; however, between the large values set for  $\sigma_{\mu_{\ell,1}}^2$  and  $\sigma_{\mu_{\ell,2}}^2$  as well as the uninformative specification induced by  $a_\ell$ , the data far outweigh the prior.

In application, we bound  $\boldsymbol{\ell}(\mathbf{s})$ ’s prior to have a support within 22.5 m in the  $x$  and  $y$  direction from  $\mathbf{s}$ . This bounding restricts the area within which the model can search for the “true” location from which  $\mathbf{z}(\mathbf{s})$  was measured. The 22.5 m bounding was used because it represents the sum of the estimated geolocation error of GEDI (10 m) and the GEDI footprint radius (12.5 m).

### 3.1 Submodel

While (2) subsumes many submodels, some of which are discussed in Section 5, the one we consider here is a model-based analog to several GEDI geolocation correction approaches, see, e.g., Quirós et al. (2021), Roy et al. (2021), and, Blair and Hofton (1999). Again using

the common local coordinate system across all  $n$  observed locations, we estimate  $\ell^* = (\ell_1^*, \ell_2^*)$  defined as the single coordinate vector that minimizes residual variance between the observed  $\mathbf{z}(\mathbf{s})$  and the additive and multiplicative adjusted  $g(\ell^*; \boldsymbol{\theta}, \text{Data}(\mathbf{s}))$ . The posited submodel is

$$\mathbf{z}(\mathbf{s}) = \boldsymbol{\alpha} + \boldsymbol{\beta} \odot g(\ell^*; \boldsymbol{\theta}, \text{Data}(\mathbf{s})) + \boldsymbol{\epsilon}(\mathbf{s}), \quad (5)$$

where parameters  $\boldsymbol{\alpha}$ ,  $\boldsymbol{\beta}$ , and  $\boldsymbol{\epsilon}(\mathbf{s})$  were defined previously for (2). The parameters' joint posterior distribution  $p(\boldsymbol{\alpha}, \boldsymbol{\beta}, \boldsymbol{\tau} \mid \mathbf{z}, \boldsymbol{\theta}, \text{Data})$  is proportional to

$$\begin{aligned} & \prod_{i=1}^n \prod_{j=1}^m \underbrace{N(z_j(\mathbf{s}_i) \mid \alpha_j + \beta_j g_j(\ell^*; \boldsymbol{\theta}, \text{Data}(\mathbf{s}_i)), \tau_j^2)}_{\text{Likelihood}} \times \\ & \prod_{j=1}^m N(\alpha_j \mid \mu_\alpha, \sigma_\alpha^2) \times \prod_{j=1}^m N(\beta_j \mid \mu_\beta, \sigma_\beta^2) \times \prod_{j=1}^m IG(\tau_j^2 \mid a_\tau, b_\tau) \times \\ & \prod_{k=1}^2 N(\ell_k^* \mid s_k, \sigma_{\ell^*,k}^2). \end{aligned} \quad (6)$$

All prior distributions, with the exception of those for elements of  $\ell^*$ , were defined previously. The prior distribution for  $\ell_1^*$  and  $\ell_2^*$  are normal with means  $s_1$  and  $s_2$ , respectively, and variances  $\sigma_{\ell^*,1}^2 = \sigma_{\ell^*,2}^2 = 1,000$ . Again, in application, we impose bounded support for  $\ell_1^*$  and  $\ell_2^*$  to be between 12.5 and 57.5 meters.

We are interested in summarizing  $\ell^*$ 's posterior distribution using its mean  $\boldsymbol{\mu}_{\ell^*}$  and MAP  $\boldsymbol{\eta}_{\ell^*}$ . As described in Section 3.2,  $\boldsymbol{\mu}_{\ell^*}$  is estimated after model fitting via composition sampling.

### 3.2 Implementation, posterior summaries, and fitted values

Models were implemented in C++ and called Fortran `openBLAS` (Zhang, 2016) and Linear Algebra Package (LAPACK; [www.netlib.org/lapack](http://www.netlib.org/lapack)) libraries for efficient matrix computations. `openBLAS` is an implementation of Basic Linear Algebra Subprograms (BLAS; [www.netlib.org/blas](http://www.netlib.org/blas)) capable of exploiting multiple processors. (*All code and data will be*

*provided on a repository to allow for reproduction of results. The code and data may be hosted by the publishing journal or public archive, and provided prior to that if requested by reviewers.)*

We refer to (2) and (5) as the *full model* and *submodel*, respectively. Inference for these models is based on samples from parameters’ posterior distributions. These samples were collected via a Markov chain Monte Carlo (MCMC) algorithm that used a Gibbs sampler for those parameters with closed form full conditional distributions (i.e.,  $\beta$ ,  $\alpha$ ,  $\tau$ ,  $\mu_\ell$  and  $\sigma_\ell$ ) and Metropolis samplers for all other parameters (see, e.g., Gelman et al., 2013, for a general description of these samplers). While developing the sampler for  $\ell$ , we found the posterior surface for a given  $\ell(\mathbf{s})$  could be highly multimodal. The posterior mode for  $\ell(\mathbf{s})$  is a location at or around  $\mathbf{s}$  that minimizes the log of the density given in (4), and hence represents a location that likely generated the observed  $\mathbf{z}(\mathbf{s})$ . We observed multiple modes in  $\ell(\mathbf{s})$ ’s posterior distribution when more than one location at or around  $\mathbf{s}$  yielded comparable values for (4) or when local modes were present. Such posterior distributions present a challenge for the basic Metropolis sampler because the MCMC chain tends to get “stuck” in local modes and fails to adequately explore the parameter space. Our solution was to use the repelling–attracting Metropolis (RAM) algorithm developed by Tak et al. (2018) that maintains the computational advantages and simple implementation of the Metropolis algorithm but allows for improved sampling from multimodal posterior distributions.

The MCMC algorithm provides samples from parameters’ posterior distributions. Posterior inference reported in Section 4 is based on  $M = 50,000$  post-convergence and thinned samples from five MCMC chains, i.e., 10,000 from each chain. We used convergence diagnostics and thinning rules outlined in Gelman et al. (2013). Point and interval estimates for  $\alpha$ ,  $\beta$ , and variance parameters presented in Section 4 include posterior medians and 95% credible intervals. Our particular interest is in estimates of  $\ell(\mathbf{s})$ s and associated  $\mu_\ell(\mathbf{s})$ s,  $\mu_\ell$ ,  $\eta_\ell(\mathbf{s})$ s, and  $\eta_\ell$  from the full model, and  $\mu_{\ell^*}$  and  $\eta_{\ell^*}$  from the submodel, because these quantities summarize the likely “true” location from which  $\mathbf{z}(\mathbf{s})$  was measured. In Section 4

we will show the distributions of  $\ell(\mathbf{s})$ s can be highly skewed, hence the full model’s means  $\mu_{\ell}(\mathbf{s})$ s and  $\mu_{\ell}$  are less useful than the MAPs  $\eta_{\ell}(\mathbf{s})$ s and  $\eta_{\ell}$  for assessing possible geolocation error.

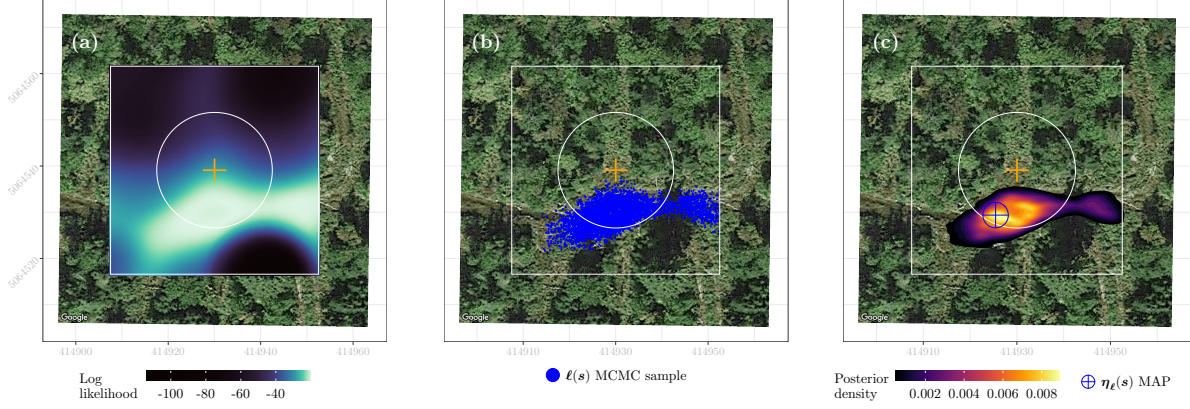


Figure 4: Continued illustration of the focal area used in Figure 2. (a) Log likelihood surface calculated using parameter point estimates from the full model. (b) Full model’s MCMC samples from  $\ell(\mathbf{s})$ ’s posterior distribution. (c) Surface plot reflecting the density of MCMC samples shown in (b), used to better visualize  $\ell(\mathbf{s})$ ’s posterior distribution and key features such as the posterior’s maximum a posteriori probability (MAP) estimate.

MCMC samples from the full models  $\ell(\mathbf{s})$ s define coordinates within the given focal area and hence can be visualized as locations on a map. The density of these samples is greater at and around locations that minimize the log of the density given in (4). This is illustrated in Figure 4 for one of the 222 focal areas and a single chain of 5,000 MCMC samples. Figure 4a shows the log likelihood surface that is generated by plugging in point estimates for  $\alpha$ ,  $\beta$ , and  $\tau$  and evaluating the log likelihood at 10,000 grid locations within the focal area (i.e., each evaluation consists of setting  $\ell(\mathbf{s})$  to a grid cell location and then computing the log likelihood). Importantly, we compute this likelihood surface only for illustrative purposes and as a “sanity check” for the MCMC-based  $\ell(\mathbf{s})$  estimates (it is used for no other purpose in the analysis). Looking at this likelihood surface, we expect samples from  $\ell(\mathbf{s})$  to be densest (i.e., sampled at a higher frequency) in regions of low log likelihood. Figure 4b shows  $\ell(\mathbf{s})$ ’s posterior sampling density follows this expectation. Using these  $\ell(\mathbf{s})$  posterior samples, we can compute point and interval estimates of the easting  $\ell_1(\mathbf{s})$  and northing  $\ell_2(\mathbf{s})$

posteriors. While such summaries of individual axes are potentially useful, we are mainly interested in the distance and direction between  $\mathbf{s}$  and  $\ell(\mathbf{s})$  modes. Given MCMC samples from  $\ell(\mathbf{s})$ 's posterior, e.g., Figure 4b, we use a two-dimensional kernel density estimation algorithm described by Venables and Ripley (2002) and implemented in the R **MASS** package to visualize  $\ell(\mathbf{s})$ 's posterior distribution and estimate its MAP location. Figure 4c shows the resulting posterior density image and MAP estimate.

Given MCMC samples from the full model's  $\ell(\mathbf{s})$ s, we generate samples from two posterior distributions of interest: 1)  $d_\ell(\mathbf{s})$  distance between each focal area's  $\ell(\mathbf{s})$  and  $\mathbf{s}$ , and 2)  $d_\ell$  distance between  $\ell(\mathbf{s})$ s across all focal areas and  $\mathbf{s}$ . Posterior samples for  $d_\ell(\mathbf{s})$  are generated using composition sampling (i.e., one sample from  $\ell(\mathbf{s})$  yields one sample from  $d_\ell$ ) via

$$\begin{aligned} d_\ell^{(l)}(\mathbf{s}) &= \left[ \left( \ell_1^{(l)}(\mathbf{s}) - s_1 \right)^2 + \left( \ell_2^{(l)}(\mathbf{s}) - s_2 \right)^2 \right]^{0.5} \\ &= \|\ell^{(l)}(\mathbf{s}) - \mathbf{s}\| \text{ for } l = (1, 2, \dots, M), \end{aligned}$$

where the superscript  $l$  in parentheses indexes MCMC samples. Similarly, samples for  $d_\ell$  are the collection of all focal area samples  $\left( d_\ell^{(l)}(\mathbf{s}_1), d_\ell^{(l)}(\mathbf{s}_2), \dots, d_\ell^{(l)}(\mathbf{s}_n) \right)$  for  $l = (1, 2, \dots, M)$ . These posteriors allow us to explore within and across focal area differences between the reported and estimated location from where  $\mathbf{z}(\mathbf{s})$  was observed.

If  $d_\ell(\mathbf{s})$ 's or  $d_\ell$ 's posterior has mass at zero, then there is evidence in support of no geolocation error. A posterior mass away from zero suggests geolocation error. A broad flat posterior that covers zero and values far from zero suggests inconclusive results. As we will see in the Section 4, such cases often occur when the focal area's vertical vegetation structure is homogeneous. In such settings, many locations might, or might not, match the observed outcome  $\mathbf{z}(\mathbf{s})$  well, with the result being a broad posterior distribution that does not identify distinctly likely locations from which  $\mathbf{z}(\mathbf{s})$  was measured.

MCMC samples from the submodel's  $\ell^*$  are used to generate samples from the posterior distribution of the distance between  $\ell^*$  and  $\mathbf{s}$ , denoted as  $d_{\ell^*}$ . Again, the desired samples

are collected using composition sampling via

$$d_{\ell^*}^{(l)} = \|\ell^{*,(l)} - \mathbf{s}\| \text{ for } l = (1, 2, \dots, M). \quad (7)$$

The  $d_{\ell^*}$  parameter is a measure of systematic geolocation error (i.e., bias) across the  $n$  focal areas. If  $d_{\ell^*}$ 's posterior has mass away from zero, then we can conclude there is systematic geolocation error. If  $d_{\ell^*}$ 's posterior has mass at zero, then we can conclude there is no systematic geolocation error, but cannot say anything about geolocation error at any given focal area. We must look to the full model's  $\ell(\mathbf{s})$ s to quantify non-systematic geolocation error.

Posterior distributions for the angle between  $\mathbf{s}$  and  $\ell(\mathbf{s})$ s and  $\ell^*$  are computed via composition sampling analogous to  $d_{\ell}(\mathbf{s})$  and  $d_{\ell^*}$ , and are useful for describing patterns in directional geolocation error.

We are also interested in quantifying the distances between  $\mathbf{s}$  and the full model's focal area specific MAP  $\boldsymbol{\eta}_{\ell}(\mathbf{s})$ s, i.e.,  $d_{\boldsymbol{\eta}_{\ell}}(\mathbf{s}_i) = \|\boldsymbol{\eta}_{\ell}(\mathbf{s}_i) - \mathbf{s}_i\|$  for  $i = (1, 2, \dots, n)$ , and cumulative MAP  $\boldsymbol{\eta}_{\ell}$ , i.e.,  $d_{\boldsymbol{\eta}_{\ell}} = \|\boldsymbol{\eta}_{\ell} - \mathbf{s}\|$ . We may also compute the direction between  $\mathbf{s}$  and the  $\boldsymbol{\eta}_{\ell}(\mathbf{s})$ s and  $\boldsymbol{\eta}_{\ell}$ .

Estimating the posterior distribution for model fitted values is a key step in assessing model fit to the observed data and geolocation error extent. Given MCMC samples from model parameters' posterior distributions, we again use composition sampling to collect samples from the model fitted value's posterior distribution. For the full model,  $M$  samples from the fitted value's posterior distribution for the  $j$ -th outcome at the  $i$ -th focal area are collected via

$$\hat{z}_j^{(l)}(\mathbf{s}_i) = N\left(\alpha_j^{(l)} + \beta_j^{(l)} g_j\left(\ell^{(l)}(\mathbf{s}_i); \boldsymbol{\theta}, \text{Data}(\mathbf{s}_i)\right), \tau_j^{2,(l)}\right) \text{ for } l = (1, 2, \dots, M). \quad (8)$$

We then compute the posterior distribution median over the  $M$  MCMC samples for each of the  $m$  outcomes and  $n$  locations. The vector of median estimates is  $\hat{\mathbf{z}} = (\hat{\mathbf{z}}(\mathbf{s}_1)^{\top}, \hat{\mathbf{z}}(\mathbf{s}_2)^{\top}, \dots, \hat{\mathbf{z}}(\mathbf{s}_n)^{\top})^{\top}$ ,

where  $\hat{\mathbf{z}}(\mathbf{s}_i) = (\hat{z}_1(\mathbf{s}_i), \hat{z}_2(\mathbf{s}_i), \dots, \hat{z}_m(\mathbf{s}_i))^\top$ . Similarly, submodel fitted values are collected using its parameters' posterior samples via

$$\hat{z}_j^{*,(l)}(\mathbf{s}_i) = N\left(\alpha_j^{(l)} + \beta_j^{(l)} g_j\left(\boldsymbol{\ell}^{*,(l)}; \boldsymbol{\theta}, \text{Data}(\mathbf{s}_i)\right), \tau_j^{2,(l)}\right) \text{ for } l = (1, 2, \dots, M), \quad (9)$$

where for all  $m$  outcomes and  $n$  focal areas, the resulting posterior distribution median estimates  $\hat{\mathbf{z}}^*$  are stacked analogous to  $\hat{\mathbf{z}}$ .

In Section 4, we compare fitted values  $\hat{\mathbf{z}}$  and  $\hat{\mathbf{z}}^*$  with the recorded GEDI measurements  $\mathbf{z}$ . We also compare the recorded GEDI measurements  $\mathbf{z}$  and simulated GEDI values at the reported GEDI footprint center location via

$$\dot{z}_j(\mathbf{s}_i) = g_j(\mathbf{s}_i; \boldsymbol{\theta}, \text{Data}(\mathbf{s}_i)). \quad (10)$$

Here, if the simulator is a good approximation for GEDI and there is no geolocation error, then  $\dot{\mathbf{z}} = (\dot{\mathbf{z}}(\mathbf{s}_1)^\top, \dot{\mathbf{z}}(\mathbf{s}_2)^\top, \dots, \dot{\mathbf{z}}(\mathbf{s}_n)^\top)^\top$ , where  $\dot{\mathbf{z}}(\mathbf{s}_i) = (\dot{z}_1(\mathbf{s}_i), \dot{z}_2(\mathbf{s}_i), \dots, \dot{z}_m(\mathbf{s}_i))^\top$ , should approximate  $\mathbf{z}$  well. If we see  $\hat{\mathbf{z}}$  and/or  $\hat{\mathbf{z}}^*$  approximate  $\mathbf{z}$  better than  $\dot{\mathbf{z}}$  then we might conclude there is some level of geolocation error. We use the root mean squared error (RMSE) between the observed  $\mathbf{z}$  and estimated  $\dot{\mathbf{z}}$ ,  $\hat{\mathbf{z}}^*$ , and  $\hat{\mathbf{z}}$  for each of the  $m$  outcomes to assess location-based fit.

## 4 Results

The two models detailed in Section 3 (the full model and submodel) were fit to the data described in Section 2. We considered  $m = 11$  RH metrics, specifically RH percentiles starting at 50 and incrementing by 5 to 95, and also 98, which we took for the canopy top height.

Estimates of  $\boldsymbol{\alpha}$  and  $\boldsymbol{\beta}$  for the full model are given in Figure 5. Following (2), if there was no geolocation error and the simulator  $g(\cdot)$  approximated  $\mathbf{z}$  well, then we would expect



elements in  $\alpha$  and  $\beta$  to be 0 and 1, respectively. Considering results given in Figure 5, we can conclude that the simulator required only marginal additive and multiplicative adjustments for the lower RH metrics. The two largest RH metrics, i.e., the 95<sup>th</sup> and 98<sup>th</sup> percentiles, corresponding estimates of  $\alpha_{10}$  and  $\alpha_{11}$ , respectively, were indistinguishable from 0, and  $\beta_{10}$  and  $\beta_{11}$ , respectively, were indistinguishable from 1. Estimates of  $\alpha$  and  $\beta$  for the submodel were similar to the full model; however, additive adjustments increased with increasing RH metrics (see, Supplementary Material Figure S1).

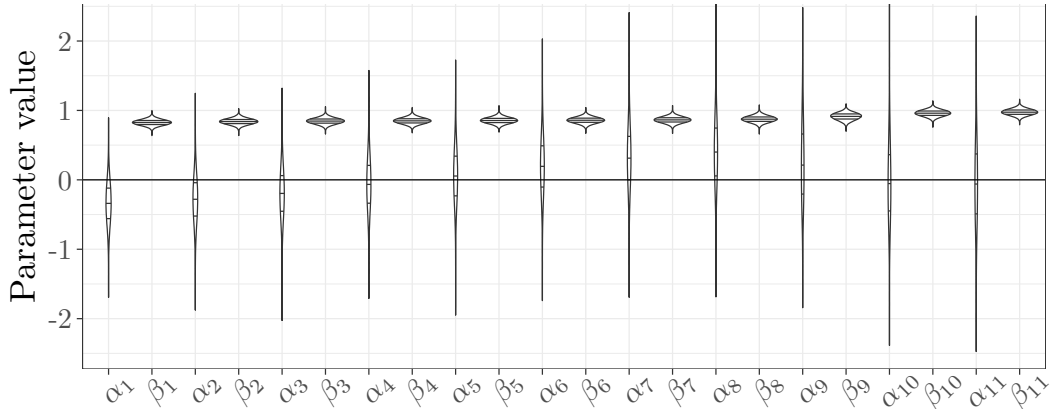


Figure 5: Posterior distribution summaries for the full model’s  $\alpha$  and  $\beta$ . The subscripts 1, 2,  $\dots$ ,  $m$ , where  $m = 11$ , correspond to relative height percentiles starting at 50 and increasing by 5 to 95, and also 98. The upper and lower horizontal lines within each violin plot represent the posterior distribution’s 95% credible bounds, and the middle horizontal line is the posterior distribution’s median. The posterior distribution range is given by the violin plot’s extremes.

Model fitted values are given in Figure 6. Here, the left subplot shows observed RH values  $\mathbf{z}(\mathbf{s})$  versus  $\hat{\mathbf{z}}(\mathbf{s})$  (i.e., simulated using  $g(\cdot)$  at the reported GEDI footprint center). As described toward the end of Section 3.2, if the simulator provides a good approximation for GEDI and there is no geolocation error, then  $\hat{\mathbf{z}}(\mathbf{s})$  should provide a good match to  $\mathbf{z}(\mathbf{s})$ . Given the shaded lines in the left subplot do not fall along the 1-to-1 line, we can conclude that either the simulator does not approximate GEDI well or there is geolocation error. It is useful to consider Figure 7, which plots RMSE between observed and fitted values by percentile, simultaneously with Figure 6. As shown by the dotted line in Figure 7, the spread

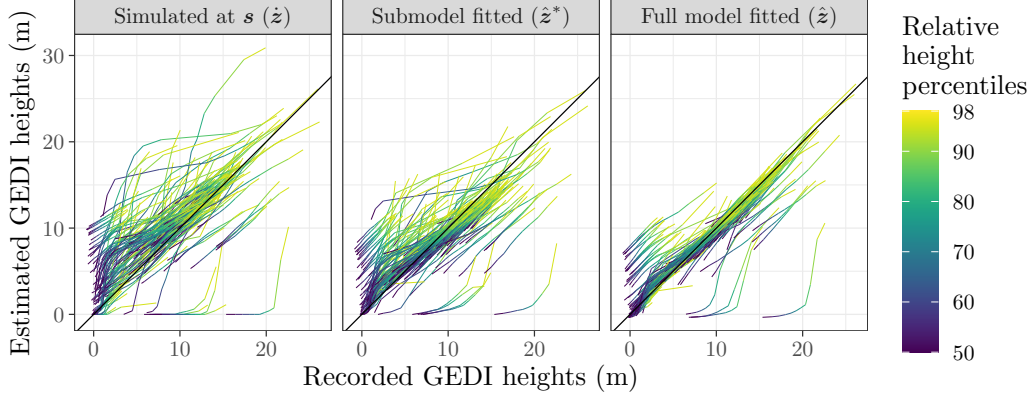


Figure 6: Each shaded line connects the  $m=11$  relative height percentiles for each of the  $n=222$  focal areas. A black 1-to-1 line is given in each subplot. Subplots from left to right are: observed versus simulated values at the reported GEDI footprint center; observed versus submodel fitted values, and; observed versus full model fitted values.

of observed versus  $\hat{z}(s)$  fitted values in Figure 6 translates to relatively large RMSE values that tend to increase with increasing RH.

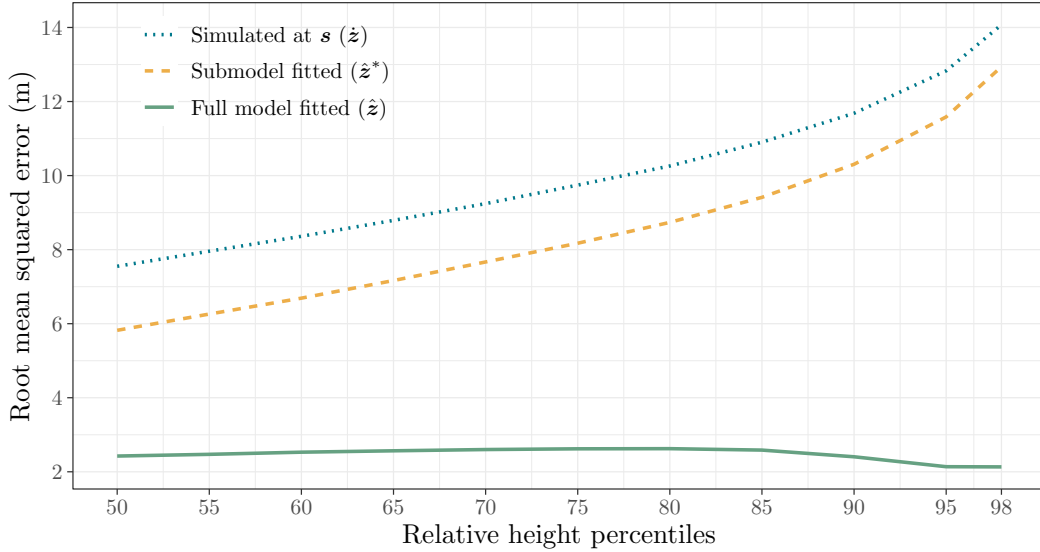


Figure 7: Root mean squared error (RMSE) between observed and fitted values. RMSE computed for each RH metric across  $n = 222$  focal areas. These RMSE values summarize the observed versus fitted values shown in Figure 6.

The middle subplot in Figure 6, and dashed line in Figure 7, show that simulating GEDI at the submodel's estimated  $\ell^*$  improves fit. The estimated posterior distribution for  $\ell^*$  is

illustrated in Figure 8(a). The posterior distribution median and 95% credible interval for elements of  $\ell^*$  are 29.57 (29.03, 30.40) and 27.27 (26.53, 28.15) for  $\ell_1^*$  and  $\ell_2^*$ , respectively. Given neither of these credible intervals overlap 35 (i.e., where 35 is the local coordinate system center coordinate and reported GEDI footprint center) we can conclude there is a substantial degree of systematic geolocation error and have a high degree of confidence the systematic error falls within the noted easting and northing credible intervals. The corresponding median and 95% credible interval estimates for  $d_{\ell^*}$  are 9.45 (8.43, 10.17) m. The estimated posterior median and 95% credible interval for the angle between  $\mathbf{s}$  and  $\ell^*$ —computed using composition sampling analogous to  $d_{\ell^*}$ —are  $234.80^\circ$  ( $230.98^\circ$ ,  $238.70^\circ$ ). As shown on Figure 8(a), the estimated MAP  $\boldsymbol{\eta}_{\ell^*}$  is 29.40 easting and 27.17 northing, which is 9.62 m from  $\mathbf{s}$  at  $234.43^\circ$ .

The right subplot in Figure 6, and solid line in Figure 7 show that simulating GEDI at the full model’s estimated  $\ell(\mathbf{s})$ s provide the best fit, relative to the reported location and submodel. The full model’s relatively tight fitted value scatter about the 1-to-1 line in Figure 6, which yields the consistently small RMSE seen in Figure 7.

The posterior distribution median and 95% credible interval for elements of  $\boldsymbol{\mu}_{\ell}$  are 33.41 (26.77, 41.09) and 33.37 (27.49, 40.14) for  $\mu_{\ell,1}$  and  $\mu_{\ell,2}$ , respectively. These estimates suggest there is no evidence of systematic geolocation error across the  $n$  focal areas (i.e., both credible intervals include 35) and, hence, runs counter to the submodel results. However,  $\ell$ ’s posterior surface and its corresponding MAP  $\boldsymbol{\eta}_{\ell}$  location shown in Figure 8(b) support the submodel result of a systematic geolocation error in the southwest direction. Specifically, the estimated MAP  $\boldsymbol{\eta}_{\ell}$  is 30.79 easting and 27.98 northing, which agrees well with the submodel  $\boldsymbol{\eta}_{\ell^*}$  estimate. This leads us to look at the interpretation of  $\boldsymbol{\mu}_{\ell}$  more closely. Figure 8(b) shows why  $\boldsymbol{\mu}_{\ell}$  is not a reliable summary of systematic error for these data. Here, histograms of  $\ell_1$ ’s and  $\ell_2$ ’s marginal posterior distributions plotted on the top and right axes of Figure 8(b), respectively, suggest substantial non-normality. These broad distributions with substantial skew cause estimates of  $\boldsymbol{\mu}_{\ell}$  to be drawn toward the focal area center and have large variability.

In contrast,  $\boldsymbol{\eta}_{\ell}$  is simply the largest value on  $\ell$ 's posterior distribution and hence not affected by deviations from normality.

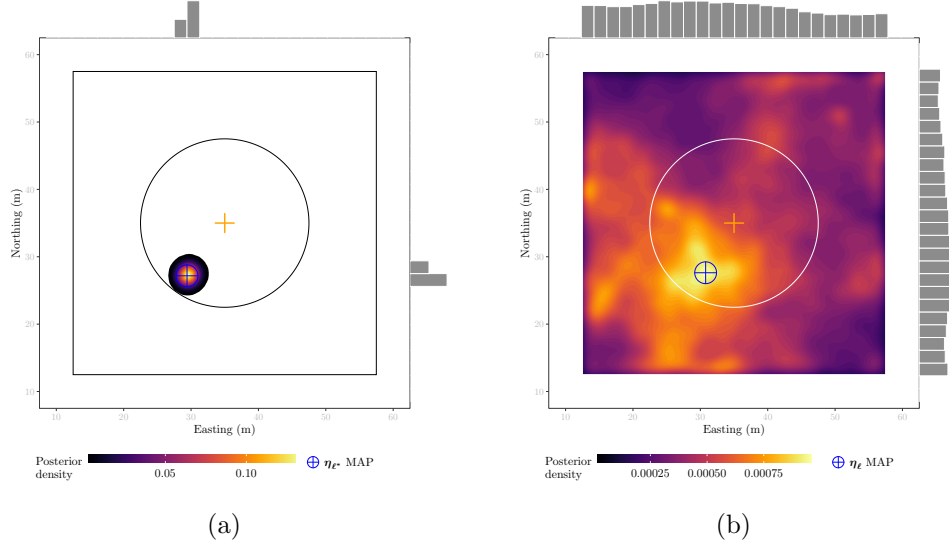


Figure 8: (a) Estimated posterior distribution surface of the submodel's  $\ell^*$ . Histograms of  $\ell_1^*$  and  $\ell_2^*$  marginal posterior distributions are plotted on the top and right axes, respectively. (b) Estimated cumulative posterior distribution surface of the full model's  $\ell(s_i)$  from  $i = (1, 2, \dots, n)$ . Histograms of  $\ell_1$ 's and  $\ell_2$ 's marginal posterior distributions are plotted on the top and right axes, respectively.

Estimates of the submodel  $\ell^*$  and  $\boldsymbol{\eta}_{\ell^*}$  and full model  $\boldsymbol{\eta}_{\ell}$  are comparable to the geolocation error of the Version 2 GEDI data reported by Dubayah et al. (2020) (i.e., approximately 10 m). However, the posterior surface in Figure 8(b) hints at geolocation error beyond this limited systematic offset, and suggests substantial geolocation error variability within and across focal areas.

When quantifying geolocation error, it is useful to distinguish between systematic error which, as defined here, is a summary of bias, and actual error which is the distance between the reported and actual measurement location. We do not have a parameter that summarizes actual geolocation error; however, we can begin to explore beyond systematic geolocation error using  $d_{\ell}$  across focal areas, and  $d_{\ell}(s)$  and  $d_{\boldsymbol{\eta}_{\ell}}(s)$  within focal areas.

Figure 9(a) summarizes  $d_{\ell}$ 's estimated posterior distribution. This distribution, and its

associated empirical cumulative distribution function (ECDF) given in Figure 9(b), suggest a relatively small portion of  $d_{\ell}$ 's posterior distribution is within 10 m of the reported footprint location. For example, the ECDF shows a  $\sim 0.2$  probability the true GEDI footprint center is within 10 m,  $\sim 0.65$  probability the true center is within 20 m, and  $\sim 0.9$  probability the true center is within 25 m.

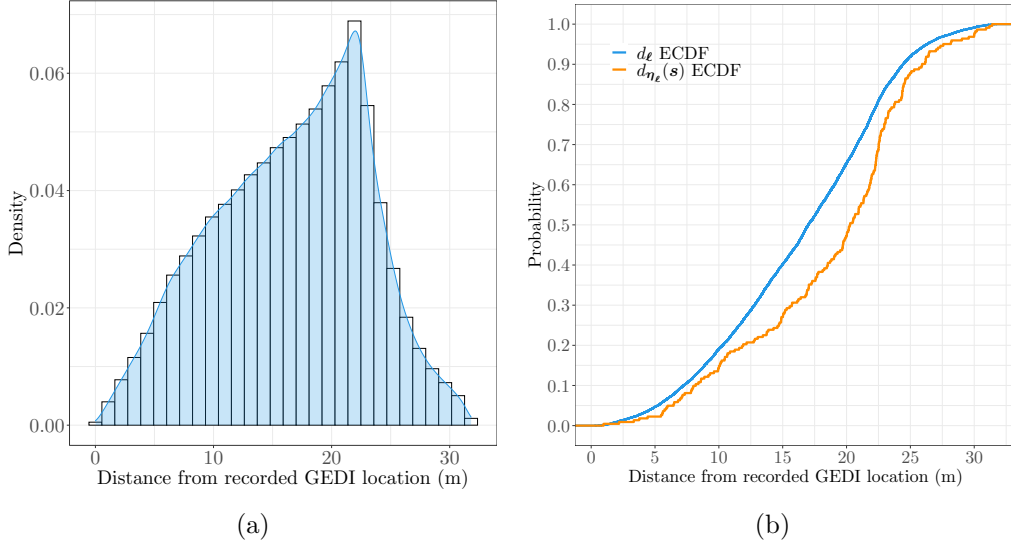


Figure 9: (a) Posterior distribution of  $d_{\ell}$ . (b) Empirical cumulative distribution function (ECDF) of  $d_{\ell}$ 's posterior distribution shown in (a) and the  $n$   $d_{\eta_{\ell}}(s)$ s.

While  $d_{\ell}$ 's distribution suggests potentially larger and more variable geolocation error beyond the estimated systematic error, it is important to recognize a limiting factor that prevents  $\ell$  and hence  $d_{\ell}$  from being a perfect summary of actual geolocation error. The issue arises when the simulator output at  $\mathbf{s}$  is the same, or very similar, to the output elsewhere in the focal area, and these outputs yield the smallest log of the density (4) across the focal area. In such settings,  $\ell(\mathbf{s})$ 's posterior distribution will have a mass over  $\mathbf{s}$  that might indicate an accurate GEDI location recording; however, the posterior will also have masses elsewhere in the focal area that yield similar  $\ell(\mathbf{s})$  posterior density values. The result is a  $d_{\ell}(\mathbf{s})$  mass at zero and the other equally likely locations within the focal area. When this occurs, results are inconclusive (i.e., we cannot tell if there is geolocation error or not) and summaries such

as given in Figure 9 include this ambiguity.

In our current analysis, the ambiguity described above occurs most often in focal areas with highly homogeneous vertical and horizontal vegetation structure. Such focal areas were noted by Roy et al. (2021) as forest types where GEDI geolocation error has smaller impact on the given analysis (which is an accurate assessment). For us, however, such settings result in inconclusive assessment of absolute geolocation error. Figures 10 and 11 illustrate focal areas 49 and 104, respectively, which each exhibit homogeneous forest structure over  $\mathbf{s}$  and hence produce broad  $d_{\ell}(\mathbf{s})$  posterior distributions as shown in Figure 12.

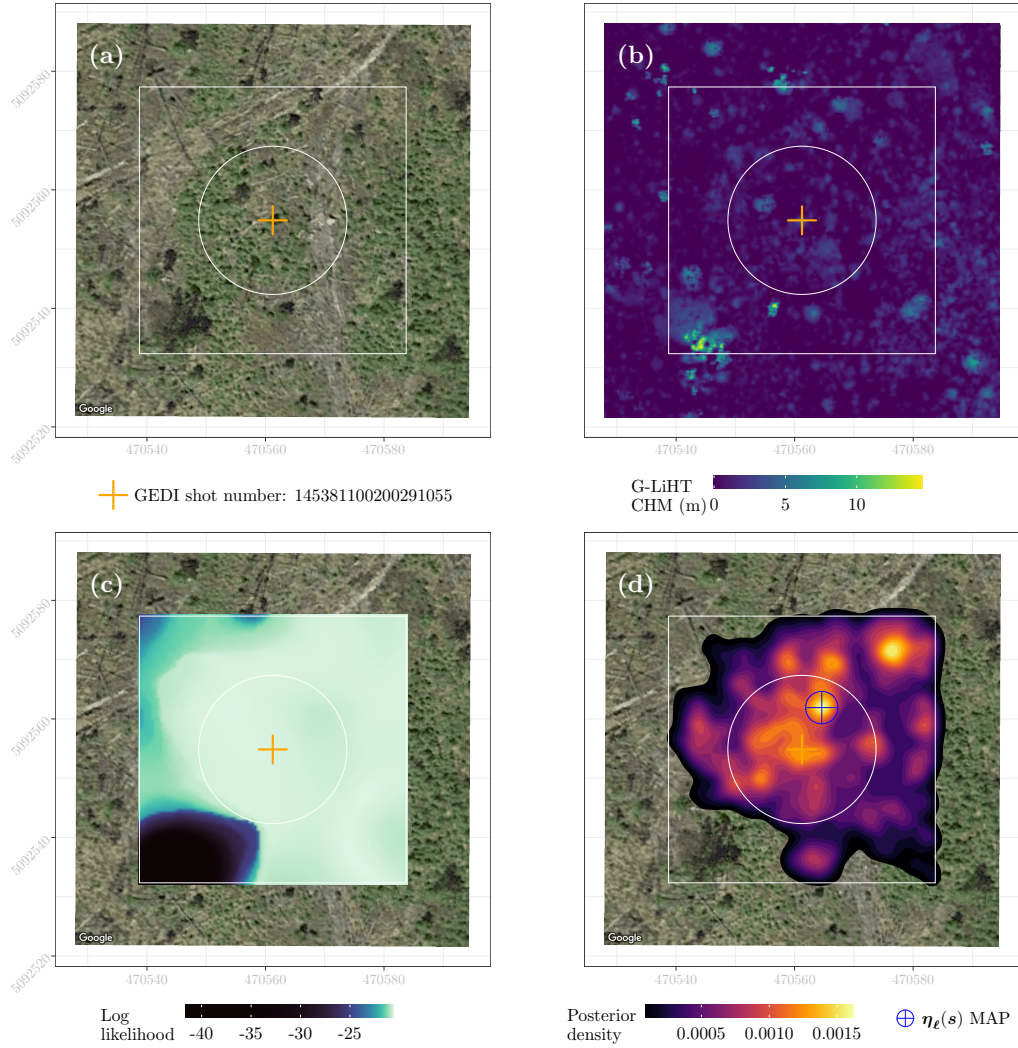


Figure 10: Example focal area 49 of 222. Illustration of a structurally homogeneous area that results in a broad posterior distribution of  $\ell(\mathbf{s})$ .



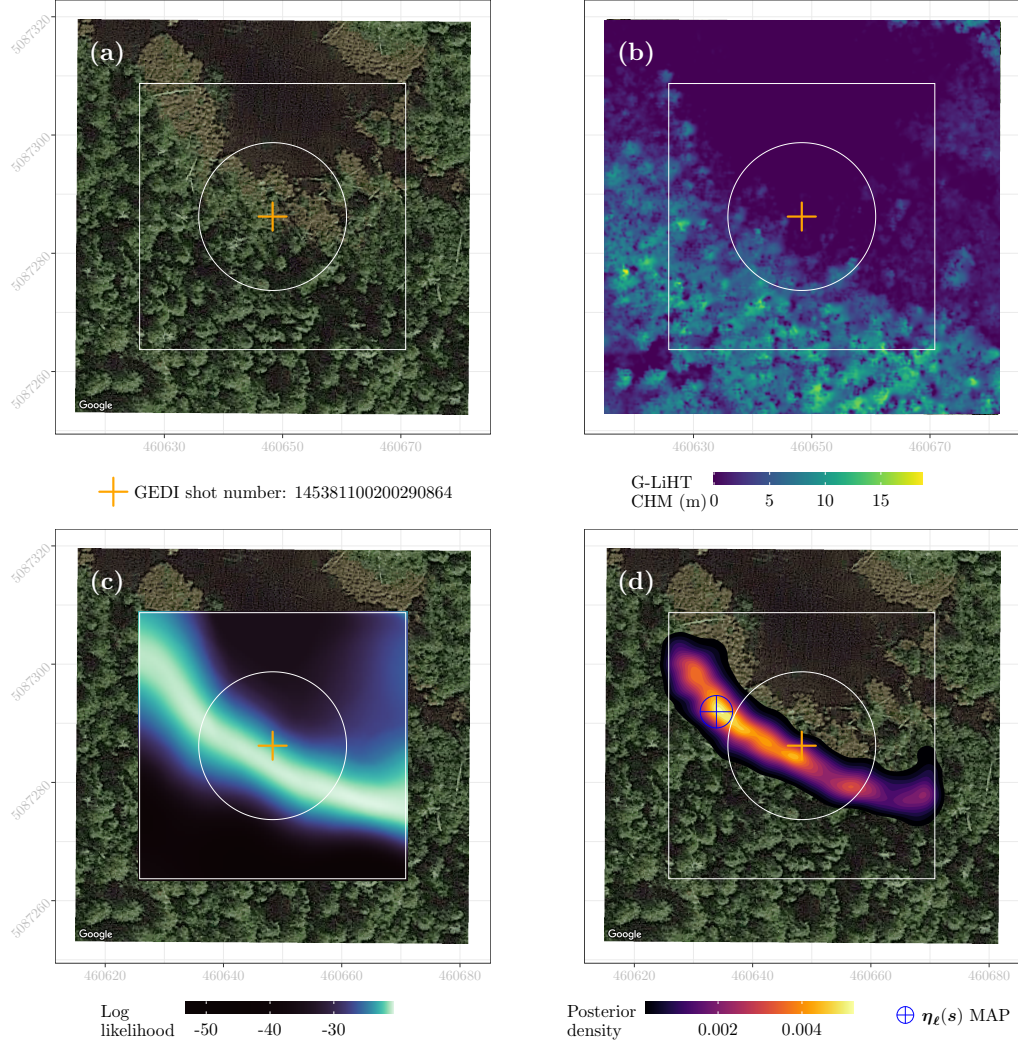


Figure 11: Example focal area 104 of 222. Illustration of a structurally homogeneous edge that results in a long and narrow posterior distribution of  $\ell(\mathbf{s})$ .

A more appropriate measure of absolute geolocation error is the focal area specific MAP  $\eta_{\ell}(\mathbf{s})$  and associated  $d_{\eta_{\ell}}(\mathbf{s})$ . These parameters do include the ambiguity associated with  $d_{\ell}(\mathbf{s})$  (e.g., as illustrated in Figures 10 and 11), they simply capture the  $\ell(\mathbf{s})$ 's MAP and distance from this MAP to the recorded GEDI footprint center. Figure 9(b) shows the ECDF for the 222  $d_{\eta_{\ell}}(\mathbf{s})$  estimates. This ECDF suggests a slightly larger absolute geolocation error than captured using  $d_{\ell}$ . For example, the  $d_{\eta_{\ell}}(\mathbf{s})$  based ECDF shows a  $\sim 0.15$  probability the true GEDI footprint center is within 10 m,  $\sim 0.45$  probability the true footprint center is within 20 m, and  $\sim 0.9$  probability the true footprint center is within 26 m.

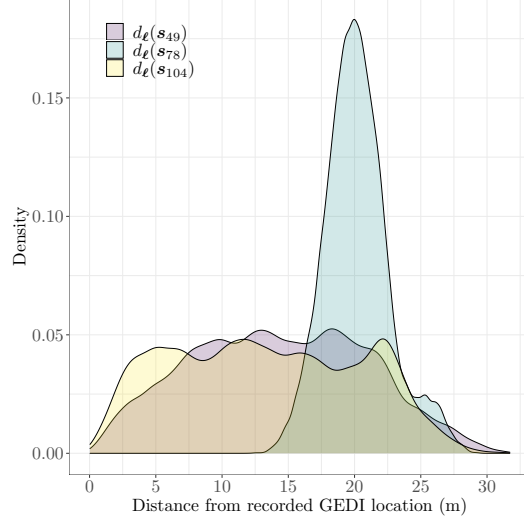


Figure 12: Estimated posterior distributions of  $d_{\ell}(\mathbf{s})$  for focal areas shown in Figures 10, 11, and 13.

As summarized in Figure 9(b), estimates of the “true” location from which  $\mathbf{z}(\mathbf{s})$  was measured are often relatively far from the recorded location. Examining each focal area’s estimates (all 222 figures of which are provided in Supplementary Material Figures S2-S223) shows diverse posterior distributions of  $\ell(\mathbf{s})$ . Some are quite broad, e.g., Figure 10, others follow contours in vertical forest structure which might or might not be apparent in the Google satellite imagery or G-LiHT data, e.g., Figure 11, while others identify very specific locations that match well the observed  $\mathbf{z}(\mathbf{s})$ , e.g., Figure 13. In cases like focal area 78, shown in Figure 13, we are provided with a relatively precise geolocation error estimate, as reflected in the corresponding posterior distribution shown in Figure 12.

## 5 Discussion

All results are conditional on the posited model. By design the submodel can only estimate systematic geolocation error. As noted in Section 3.1, the submodel is a model-based analog to methods used in several similar studies that sought to estimate an “optimal” GEDI footprint location correction. These alternative methods simulated GEDI using ALS data



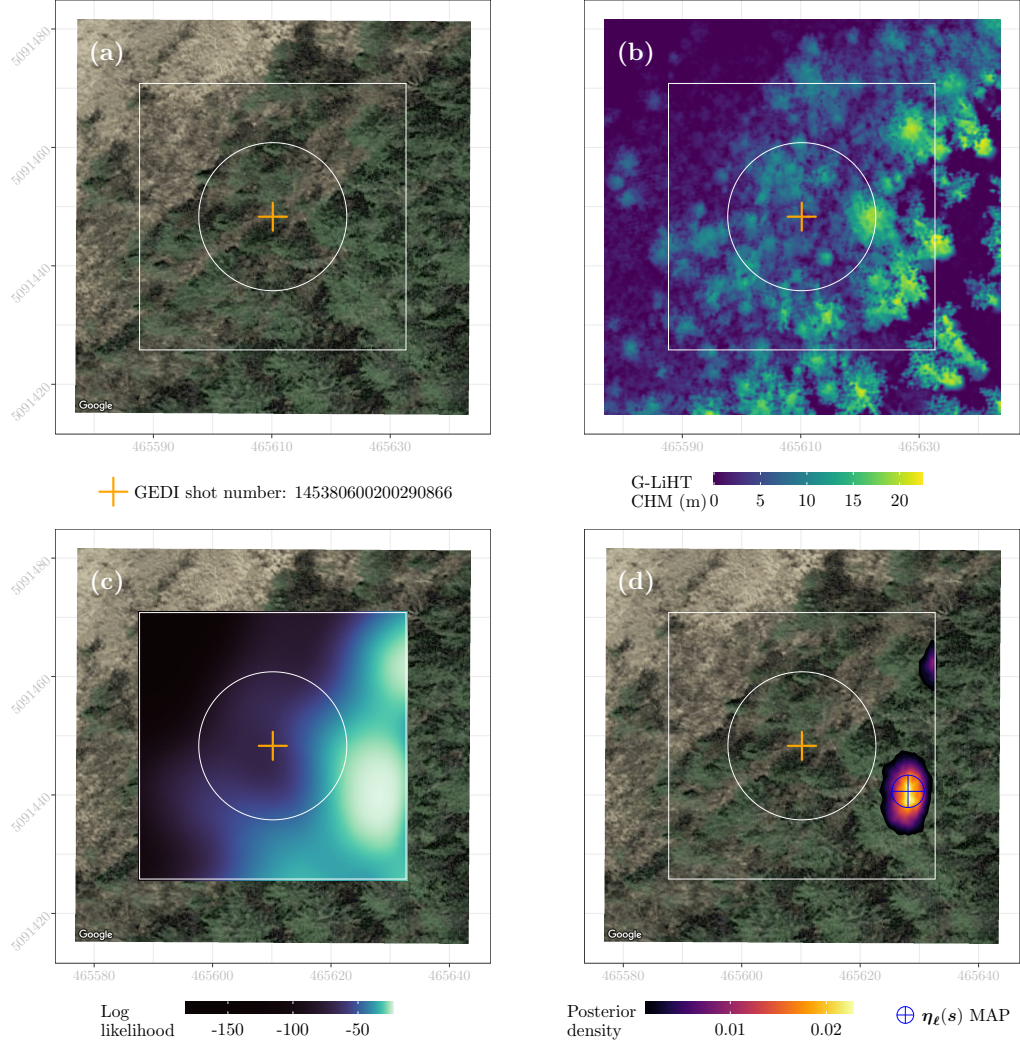


Figure 13: Example focal area 78 of 222. Illustration of posterior distribution of  $\ell(\mathbf{s})$  concentrated well away from the reported footprint center location.

for a finite number of locations at and around the recorded GEDI footprint center. The optimal location was then selected via an objective function that considered both the observed and simulated GEDI data. In spirit, our proposed method is similar to these previous approaches. Here, for the submodel, we discover the “optimal” location by minimizing the log of (6) and selecting a summary measure, e.g., mean, median, or MAP, of the estimated  $\ell^*$ ’s posterior distribution. For the full model, minimizing the log of (4) yields estimated posterior distributions of  $\ell(\mathbf{s}_i)$  for  $i = (1, 2, \dots, n)$  from which we can glean “optimal” systematic error correction via  $\eta_{\ell}$  and local error correction via  $\eta_{\ell}(\mathbf{s}_i)$ s. By using a Bayesian

inferential paradigm, we have access to full posterior distributions and can hence deliver full probabilistic error quantification for  $\ell(\mathbf{s}_i)$ s, derived parameters (e.g.,  $d_\ell(\mathbf{s}_i)$ s and  $\mathbf{z}$  fitted values), and all other model parameters.

Our results suggest that the non-normality of  $\ell$ 's posterior distribution reduces the usefulness of estimating  $\mu_\ell$  in the full model, and that  $\eta_\ell$  is a more appropriate measure of systematic geolocation error. It is still useful to center the  $\ell(\mathbf{s})$ 's on  $\mathbf{s}$  (which places prior weight on the assumption that the reported GEDI footprint center location is accurate). Hence, an attractive alternative specification of (3) is  $\ell(\mathbf{s}) = \mathbf{s} + \epsilon_\ell(\mathbf{s})$  which replaces the last line in (4) with  $\prod_{i=1}^n \prod_{k=1}^2 N(\ell_k(\mathbf{s}_i) | s_k, 1000)$ . Removing  $\mu_\ell$  and associated hyperpriors yields a more parsimonious model and might, in some settings, improve numerical algorithm convergence used to estimate parameters. We have fit this alternative specification and it yields nearly identical results to the full model detailed in Section 3.

There is geolocation error in the reported GEDI data considered here and summaries of systematic geolocation error do not reflect well the actual error apparent in most focal areas (i.e., those focal areas where the  $\ell(\mathbf{s})$ 's posterior mass is distinct from  $\mathbf{s}$ ). Attempting to address geolocation error by shifting GEDI footprint locations to the  $\ell^*$ 's mean, median, or MAP will provide only marginal improvement in fit as reflected by the middle subplot in Figure 6. While there was clear systematic error, there was also large variation in actual error across GEDI footprint locations. This large variation has implications for studies that attempt to spatially coincide GEDI data with other remotely sensed or georeferenced field measurements.

## 6 Summary and future work

We propose a general model to estimate geolocation error in sampling LiDAR using a simulator function that takes a set of potentially unknown parameters and spatially coinciding high spatial accuracy ALS data. The model accommodates multiple canopy height metrics, can

estimate unknown parameters in the simulator function, and provides additive and multiplicative correction when mapping between the observed and simulated LiDAR metrics. The key feature of the proposed model is its ability to deliver probabilistic estimates of actual and systematic geolocation error via a rich, flexible, and extendable Bayesian framework.

We motivate and illustrate the proposed model using GEDI and G-LiHT ALS data from Northern Maine, USA. Our results indicate some degree of systematic geolocation error over all GEDI footprint locations, with more variability in the actual geolocation error across locations. For this initial study, the spatial and temporal scope were kept intentionally narrow to minimize confounding effects of spatial and temporal variability. In the future, the full or submodel can be extended to include both spatial or temporal random effects on  $\ell(\mathbf{s})$ s and  $\ell^*$ , respectively, designed to capture differences among acquisitions across locations and dates. The full model random effects can also be written to accommodate spatially and/or temporally structured  $\ell(\mathbf{s})$ s that would allow for estimation of correlation among actual errors. If such spatial or temporal correlation exists, then the full model could be used to correct geolocation error in regions where no ALS data exist.

## Acknowledgements

Funding was provided by: NASA Carbon Monitoring System (CMS) grants Hayes (CMS 2020) and Cook (CMS 2018), National Science Foundation (NSF) DMS-1916395, and a joint venture agreement with the USDA Forest Service Forest Inventory and Analysis.

## References

- Blair, J. B. and Hofton, M. A. (1999). Modeling laser altimeter return waveforms over complex vegetation using high-resolution elevation data. *Geophysical Research Letters*, 26(16):2509–2512.
- Cohen, W., Yang, Z., Healey, S., and Andersen, H. (2020). Disturbance history and forest biomass from landsat for six us sites, 1985-2014. ORNL Distributed Active Archive Center. doi: 10.3334/ornl daac/1679.
- Cook, B. D., Corp, L. A., Nelson, R. F., Middleton, E. M., Morton, D. C., McCorkel, J. T., Masek, J. G., Ranson, K. J., Ly, V., and Montesano, P. M. (2013). NASA Goddard’s Lidar, Hyperspectral and Thermal (G-LiHT) Airborne Imager. *Remote Sensing*, 5(8):4045–4066.
- Deo, R. K., Russell, M. B., Domke, G. M., Andersen, H.-E., Cohen, W. B., and Woodall, C. W. (2017). Evaluating site-specific and generic spatial models of aboveground forest biomass based on landsat time-series and lidar strip samples in the eastern usa. *Remote Sensing*, 9(6).
- Dubayah, R., Blair, J. B., Goetz, S., Fatoyinbo, L., Hansen, M., Healey, S., Hofton, M., Hurtt, G., Kellner, J., Luthcke, S., Armston, J., Tang, H., Duncanson, L., Hancock, S., Jantz, P., Marselis, S., Patterson, P. L., Qi, W., and Silva, C. (2020). The global ecosystem dynamics investigation: High-resolution laser ranging of the earth’s forests and topography. *Science of Remote Sensing*, 1:100002.
- Dubayah, R., Hofton, M., Blair, J., Armston, J., Tang, H., and Luthcke, S. (2021). GEDI L2A elevation and height metrics data global footprint level v002 [data set]. NASA EOSDIS Land Processes DAAC.
- Duncanson, L., Kellner, J. R., Armston, J., Dubayah, R., Minor, D. M., Hancock, S., Healey, S. P., Patterson, P. L., Saarela, S., Marselis, S., Silva, C. E., Bruening, J., Goetz, S. J.,

Tang, H., Hofton, M., Blair, B., Luthcke, S., Fatoyinbo, L., Abernethy, K., Alonso, A., Andersen, H.-E., Aplin, P., Baker, T. R., Barbier, N., Bastin, J. F., Biber, P., Boeckx, P., Bogaert, J., Boschetti, L., Boucher, P. B., Boyd, D. S., Burslem, D. F., Calvo-Rodriguez, S., Chave, J., Chazdon, R. L., Clark, D. B., Clark, D. A., Cohen, W. B., Coomes, D. A., Corona, P., Cushman, K., Cutler, M. E., Dalling, J. W., Dalponte, M., Dash, J., de Miguel, S., Deng, S., Ellis, P. W., Erasmus, B., Fekety, P. A., Fernandez-Landa, A., Ferraz, A., Fischer, R., Fisher, A. G., García-Abril, A., Gobakken, T., Hacker, J. M., Heurich, M., Hill, R. A., Hopkinson, C., Huang, H., Hubbell, S. P., Hudak, A. T., Huth, A., Imbach, B., Jeffery, K. J., Katoh, M., Kearsley, E., Kenfack, D., Kljun, N., Knapp, N., Král, K., Krůček, M., Labrière, N., Lewis, S. L., Longo, M., Lucas, R. M., Main, R., Manzanera, J. A., Martínez, R. V., Mathieu, R., Memiaghe, H., Meyer, V., Mendoza, A. M., Monerri, A., Montesano, P., Morsdorf, F., Næsset, E., Naidoo, L., Nilus, R., O'Brien, M., Orwig, D. A., Papathanassiou, K., Parker, G., Philipson, C., Phillips, O. L., Pisek, J., Poulsen, J. R., Pretzsch, H., Rüdiger, C., Saatchi, S., Sanchez-Azofeifa, A., Sanchez-Lopez, N., Scholes, R., Silva, C. A., Simard, M., Skidmore, A., Stereńczak, K., Tanase, M., Torresan, C., Valbuena, R., Verbeeck, H., Vrska, T., Wessels, K., White, J. C., White, L. J., Zahabu, E., and Zraggen, C. (2022). Aboveground biomass density models for NASA’s Global Ecosystem Dynamics Investigation (GEDI) lidar mission. *Remote Sensing of Environment*, 270:112845.

Frazer, G., Magnussen, S., Wulder, M., and Niemann, K. (2011). Simulated impact of sample plot size and co-registration error on the accuracy and uncertainty of lidar-derived estimates of forest stand biomass. *Remote Sensing of Environment*, 115(2):636–649.

Gelman, A., Carlin, J., Stern, H., Dunson, D., Vehtari, A., and Rubin, D. (2013). *Bayesian Data Analysis, Third Edition*. Chapman & Hall/CRC Texts in Statistical Science. Taylor & Francis.

Goward, S. N., Masek, J. G., Cohen, W., Moisen, G., Collatz, G. J., Healey, S., Houghton,

- R. A., Huang, C., Kennedy, R., Law, B., Powell, S., Turner, D., and Wulder, M. A. (2008). Forest disturbance and north american carbon flux.
- Hancock, S., Armston, J., Hofton, M., Sun, X., Tang, H., Duncanson, L. I., Kellner, J. R., and Dubayah, R. (2019). The GEDI simulator: A large-footprint waveform lidar simulator for calibration and validation of spaceborne missions. *Earth and Space Science*, 6(2):294–310.
- Lang, N., Kalischek, N., Armston, J., Schindler, K., Dubayah, R., and Wegner, J. D. (2022). Global canopy height regression and uncertainty estimation from GEDI lidar waveforms with deep ensembles. *Remote Sensing of Environment*, 268:112760.
- Liu, A., Cheng, X., and Chen, Z. (2021). Performance evaluation of GEDI and ICESat-2 laser altimeter data for terrain and canopy height retrievals. *Remote Sensing of Environment*, 264:112571.
- Milenković, M., Schnell, S., Holmgren, J., Ressl, C., Lindberg, E., Hollaus, M., Pfeifer, N., and Olsson, H. (2017). Influence of footprint size and geolocation error on the precision of forest biomass estimates from space-borne waveform lidar. *Remote Sensing of Environment*, 200:74–88.
- Quirós, E., Polo, M.-E., and Fragoso-Campón, L. (2021). GEDI elevation accuracy assessment: A case study of southwest spain. *IEEE Journal of Selected Topics in Applied Earth Observations and Remote Sensing*, 14:5285–5299.
- Roy, D., Kashongwe, H., and Armston, J. (2021). The impact of geolocation uncertainty on GEDI tropical forest canopy height estimation and change monitoring. *Science of Remote Sensing*, 4(100024).
- Saarela, S., Holm, S., Healey, S. P., Andersen, H.-E., Petersson, H., Prentius, W., Patterson, P. L., Næsset, E., Gregoire, T. G., and Ståhl, G. (2018). Generalized hierarchical model-

- based estimation for aboveground biomass assessment using GEDI and Landsat data. *Remote Sensing*, 10(11).
- Silva, C. A., Duncanson, L., Hancock, S., Neuenschwander, A., Thomas, N., Hofton, M., Fatoyinbo, L., Simard, M., Marshak, C. Z., Armston, J., Lutchke, S., and Dubayah, R. (2021). Fusing simulated GEDI, ICESat-2 and NISAR data for regional aboveground biomass mapping. *Remote Sensing of Environment*, 253:112234.
- Tak, H., Meng, X.-L., and van Dyk, D. A. (2018). A repelling–attracting metropolis algorithm for multimodality. *Journal of Computational and Graphical Statistics*, 27(3):479–490.
- Venables, W. N. and Ripley, B. D. (2002). *Modern Applied Statistics with S*. Springer, New York, fourth edition. ISBN 0-387-95457-0.
- Wang, C., Elmore, A. J., Numata, I., Cochrane, M. A., Shaogang, L., Huang, J., Zhao, Y., and Li, Y. (2022). Factors affecting relative height and ground elevation estimations of GEDI among forest types across the conterminous usa. *GIScience & Remote Sensing*, 59(1):975–999.
- Zhang, X. (2016). An optimized blas library based on gotoblas2. <https://github.com/xianyi/OpenBLAS/>. Accessed 2015-06-01.